Electron slowing-down spectra in aluminum metal*

C. J. Tung† and R. H. Ritchie
Health and Safety Research Division, Oak Ridge National Laboratory, Oak Ridge, Tennessee 37830
and Department of Physics and Astronomy, The University of Tennessee, Knoxville, Tennessee 37916
(Received 29 June 1977)

We have studied theoretically the energy distribution of electrons generated in solid aluminum by uniformly distributed electron sources of various energies. Inelastic cross sections for energy loss and secondary electron creation are inferred from the electron-gas model for those electrons which are in the conduction band. Inner-shell excitations are treated using atomic models. Slowing-down spectra are computed for several monoenergetic sources and for β particles from the decay of radioactive ^{198}Au. Comparison with experimental data is made.

I. INTRODUCTION

The distribution in energy of electrons generated in condensed matter by ionizing radiation is of much interest in radiation physics. A theory of electron slowing-down in matter was first formulated and used for practical calculations by Spencer and Fano.[1-3] The Møller cross section for electron-electron scattering was employed to compute the δ-ray flux generated by electrons interacting with the medium. This flux when added to the flux of electrons slowing down from higher energies gives the total flux in the medium at arbitrary energy. The Spencer-Fano approach as originally employed is strictly valid only for energies large compared with the binding energies of the most tightly-bound electrons in the medium. At energies of the order of tens of rydbergs, even in low-Z materials such as aluminum and silicon, the Møller cross section is inadequate to describe δ-ray distributions in single collisions. Following this work, slowing-down spectra in gases were computed by Platzman and his collaborators[4-6] and used by them to determine, among other things, the average energy required to produce an ion pair by heavy charged particles. Although electron slowing-down spectra in solids should be intrinsically more difficult to measure than the corresponding quantities in gases, extensive measurements have been carried out on the former. Birkhoff and his co-workers[7,8] for some time have been making such measurements using the Keplertron, a spherical electrostatic electron spectrometer with unusually high transmission characteristics, which they designed and constructed.

In this work, we have solved the Boltzmann transport equation to obtain numerical values of the slowing-down flux for both monoenergetic sources and for β particles from the decay of radioactive ^{198}Au in the medium of Al metal. We have employed the electron-gas model to obtain differential inverse mean free paths for electrons of various energies interacting with the valence electrons in Al. Inner-shell excitations are described by atomic models and evaluated within the Born approximation. The distribution in energy of Auger electrons from the filling of inner-shell vacancies is also estimated.

II. STATISTICAL BALANCE EQUATION FOR ELECTRONS

Energetic electrons with energies of the order of rydbergs created throughout a medium will be scattered into lower-energy states through inelastic collisions with the electrons and ions constituting the medium. At the same time, a great number of secondary electrons with much smaller energies will be generated. If the medium is isotropic and uniform, and source electrons are born at a constant rate, attention may be focused only on the energy dependence of the slowing-down spectrum regardless of its variation with space and time. Electron slowing-down spectra are ordinarily treated theoretically using the Monte-Carlo method or the Boltzmann transport equation method. We will discuss the transport equation method here.

Suppose there are $N(E)dE$ electrons born per unit volume in the medium in the infinitesimal energy range between E and $E+dE$. The equation that expresses the statistical balance between electrons produced in this range and electrons scattered out through inelastic collision processes is given by

$$\phi(E)\,dE\int_0^\infty \tau(E,E')\,dE' = N(E)\,dE + \int_E^\infty dE'\,\phi(E')\,[\tau(E',E'-E) + \tau_s(E',E)]\,dE\,, \quad (1)$$

where $\phi(E)\,dE$ represents the electron flux at the

energy range between E and $E+dE$. $\tau(E,E')$ is the differential inverse mean free path (DIMFP) and describes the probability per unit path length for an electron with energy E to lose energy E' per unit energy through interactions with the medium. $\tau_s(E',E)$ is the DIMFP for an electron with energy E' to generate a secondary electron with energy E per unit energy interval about E.

In the case of inner shells, it is assumed that the binding energies associated with each shell have negligible widths and that the DIMFP for the production of secondary electrons from a given ith shell may be written as

$$\tau_{si}(E',E)=\tau_i(E',E+\hbar\omega_B^i)\,, \tag{2}$$

where $\hbar\omega_B^i$ is the binding energy of the ith shell.

The contribution of Auger electrons generated in the filling of vacancies in inner shells may be included as an additional source term in Eq. (1). The details of this procedure are discussed below.

III. ELECTRON INELASTIC COLLISIONS IN ALUMINUM METAL

A swift electron traveling in a solid may lose energy to the medium through numerous types of inelastic collision processes. For instance, radiative losses may become important at relativistic velocities.[9] On the other hand, the most important interactions for very-low-energy electrons (~1 eV) may be the generation of phonons and electron-hole pairs in the immediate vicinity of the Fermi level. In the energy region considered here, from the Fermi level to ~1 MeV, the significant energy losses by an energetic electron are assumed to be due to electron-electron interactions which give rise to the generation of electron-hole pairs, collective oscillations, and inner-shell excitations and ionizations.

In this work, we have treated electrons in the conduction band using an electron-gas model. Electrons belonging to inner shells are studied using numerically specified atomic generalized oscillator strength (GOS) functions obtained from theory.

A. Differential inverse mean free paths

1. Conduction band

Lindhard's pioneering work on the electron gas[10] has had much impact on solid-state physics. His dielectric function is known to represent in a reasonable way the response of electrons in the conduction band of free-electron-like metals to external perturbations. Even though it is derived from a first-order, self-consistent, time-dependent Hartree approach, it has been shown that many-body corrections to Lindhard's dielectric function do not affect in an important way calculations of the stopping power of an electron gas,[11,12] nor calculations of electron inelastic inverse mean free path[13,14] made with it.

In the Born approximation, the DIMFP for an electron with energy ϵE_F to transfer energy xE_F to the electron gas is given by[15]

$$\tau(\epsilon,x)=\frac{1}{\pi a_0}\frac{\Theta(\epsilon-x)}{(\epsilon+1)}\int_{z_-}^{z_+}\frac{dz}{z}\,\mathrm{Im}\left(\frac{-1}{\epsilon^L_{z,x}}\right), \tag{3}$$

where $z_\pm=\frac{1}{2}[(\epsilon+1)^{1/2}\pm(\epsilon+1-x)^{1/2}]$. The step function $\Theta(\epsilon-x)$ ensures that no electrons lose enough energy to fall below the Fermi level. Also $z=k/2k_F$, $x=\hbar\omega/E_F$, $\hbar k$ is the momentum transfer, $\hbar\omega$ is the energy transfer, a_0 is the Bohr radius, $\epsilon^L_{z,x}$ is the Lindhard dielectric function of the electron gas, and $\hbar k_F$ and E_F are the Fermi momentum and energy, respectively. Note that all energies here are measured from the Fermi level and in units of the Fermi energy. The integration over z in Eq. (3) is restricted to the region in which energy and momentum transfers by the incident electron are compatible and in which the Pauli exclusion principle is satisfied.

The function $\epsilon^L_{z,x}$ satisfies the basic sum rules

$$\int_0^\infty x\,\mathrm{Im}(\epsilon^L_{z,x})\,dx=\tfrac{1}{2}\pi x_p^2 \tag{4}$$

and

$$\int_0^\infty x\,\mathrm{Im}\left(\frac{-1}{\epsilon^L_{z,x}}\right)dx=\tfrac{1}{2}\pi x_p^2\,, \tag{5}$$

where $x_p^2=(4\pi\hbar^2ne^2/m)/E_F^2$ and n is the density of electrons in the electron gas.

The Lindhard dielectric function may be written explicitly as

$$\epsilon^L_{z,x}=1+(\chi^2/z^2)[f_1(x,z)+if_2(x,z)]\,, \tag{6}$$

where $\chi^2=(\pi a_0k_F)^{-1}$,

$$f_1(x,z)=\tfrac{1}{2}+\frac{1}{8z}\left[1-\left(z-\frac{x}{4z}\right)^2\right]\ln\left|\frac{z-x/4z+1}{z-x/4z-1}\right|$$
$$+\frac{1}{8z}\left[1-\left(z+\frac{x}{4z}\right)^2\right]\ln\left|\frac{z+x/4z+1}{z+x/4z-1}\right|,$$

and $f_2(x,z)=\pi x/8z$ in region I; $(\pi/8z)[1-(z-x/4z)^2]$ in region II; 0 in region III. Region I is bounded by the lines $x=0$ and $x=4z(1-z)$. Region II is bounded by $x=4z(1-z)$, $x=4z(z+1)$, and $x=4z(z-1)$. Region III consists of the remaining part of the zx plane. Figure 1 shows these three regions in the zx plane. The dot-dash line in Fig. 1 shows a representative energy-momentum compatibility curve for the incident electron, $x=4z[(\epsilon+1)^{1/2}-z]$, for a particular energy $\epsilon=8$. Energy and momentum transfers are allowed for all val-

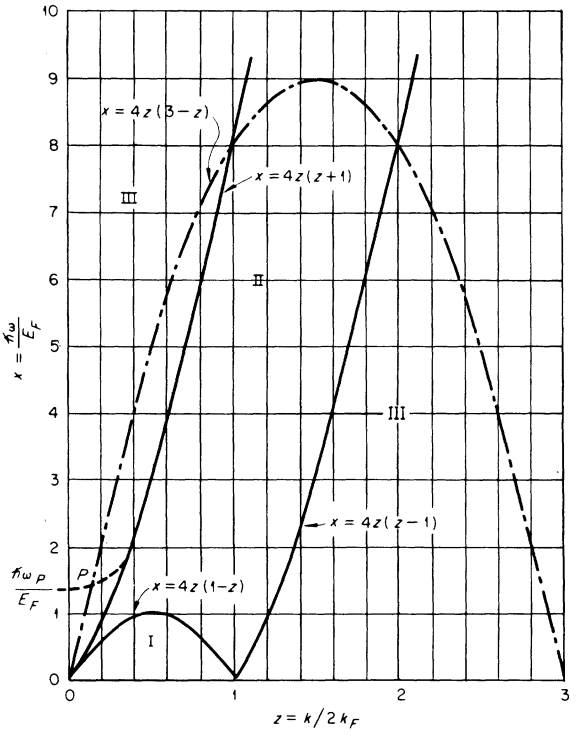

FIG. 1. Regions of the zx plane in which different representations of the imaginary part of the electron gas dielectric function $\epsilon_2(x,z)$ must be used.

ues of z and x lying below this curve.

Two distinct physical contributions arise from integrations of Eq. (3) over different regions of the zx plane. In regions I and II, where $f_2(x,z)\neq 0$, the contribution is due to excitations of single electron-hole pairs. The DIMFP function for these excitations τ_{ee} may be calculated immediately from the relation

$$\tau_{ee}(\epsilon,x) = \frac{\chi^2}{\pi a_0}\frac{\Theta(\epsilon-x)}{(\epsilon+1)} \times \int_{[(x+1)^{1/2}-1]/2}^{[(x+1)^{1/2}+1]/2} \frac{z f_2(x,z)\,dz}{[z^2+\chi^2 f_1(x,z)]^2+\chi^4 f_2^2(x,z)}, \tag{7}$$

where the limits on the z integration correspond to values lying in regions I and II.

Equation (7) shows that the function $(\epsilon+1)\tau_{ee}(\epsilon,x)$ is independent of the incident electron energy ϵ except for its presence in the argument of the step function. Figure 2 shows a plot of this function against x for several different electron gas densities. The density corresponding to a given curve in the figure is characterized by its r_s value. This useful quantity represents the radius of a sphere, in units of a_0, containing on the average one electron in the electron gas and is defined by $n=[\frac{4}{3}\pi(a_0 r_s)^3]^{-1}$, where n is the electron gas density. In these terms $\chi^2=(\frac{4}{9}\pi^4)^{1/3}r_s$. We take the conduction band of aluminum to correspond to an electron gas with $r_s=2.07$. For very large values of x, the DIMFP function follows a x^{-2} law, a characteristic behavior for the case of collisions with completely free electrons.

In region III where $f_2(x,z)=0$, the integration of Eq. (3) gives a nonzero contribution only in the neighborhood of the plasma dispersion line and represents the contribution from plasma oscillations of the electron gas. One may expand the real part of ϵ^L in the denominator of Eq. (3) as a power series about the plasma line, assume that $\mathrm{Im}(\epsilon^L)$ is a positive infinitesimal, and then evaluate the z integral in terms of the derivative of ϵ^L at the plasma resonance. One obtains in this way the DIMFP for plasma excitations

$$\tau_p(\epsilon,x) = \frac{1}{a_0}\frac{\Theta(\epsilon-x)}{(\epsilon+1)}\frac{z_0}{|\partial F/\partial z|_{z_0}}\Theta(x-x_{\min}) \times\Theta(x_{\max}-x), \tag{8}$$

where $F=z^2+\chi^2 f_1(x,z)$, and the plasma resonance line $z_0(x)$ is defined by $F(z_0,x)=0$. The additional step functions introduced in Eq. (8) represent, respectively, the minimum energy that an incident electron can lose without violating the energy-momentum compatibility condition and the maximum energy that plasmons can possess without decaying into electron-hole pairs. It is readily seen from Fig. 1 that $x_{\min}$ and $x_{\max}$ are determined from the

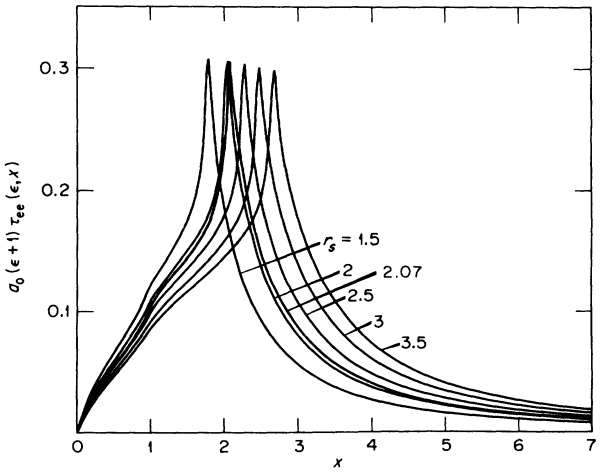

FIG. 2. Plot of $a_0(\epsilon+1)\tau_{ee}(\epsilon,x)$ vs x in electron gases of various densities. Here $\tau_{ee}(\epsilon,x)$ is the differential inverse mean free path for energy loss xE_F to electron-hole pair excitation in an electron gas by a primary electron of energy ϵE_F.

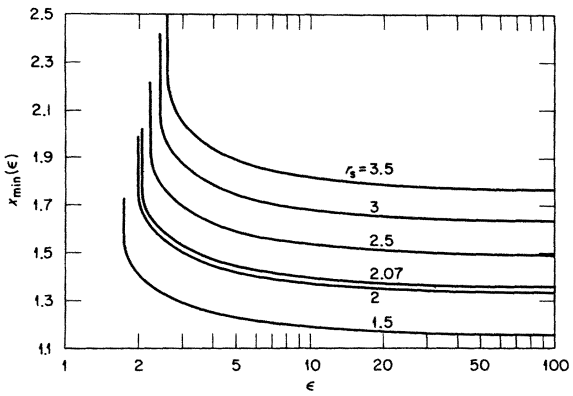

FIG. 3. Plot of x_{min} vs ϵ for various electron gas densities. Here x_{min} is the minimum energy loss needed to generate a plasmon in the gas by an electron with energy ϵ.

relations $x_{min}=4z_0(x_{min})[(\epsilon+1)^{1/2}-z_0(x_{min})]$ and $x_{max}=4z_0(x_{max})[1+z_0(x_{max})]$. Figure 3 shows a plot of x_{min} vs ϵ for various electron gas densities. These curves indicate that electrons with energy smaller than $x_{min}E_F$ are unable to generate plasmons in the system. This is, of course, only true when the plasmon damping is neglected. For very large values of ϵ, the approximate relation $x_{min} \approx 1.3558+0.412/\epsilon$ for the case $r_s=2.07$ is useful. The maximum energy transfer x_{max} in this case has the value ~2.02.

Figure 4 shows a plot of $a_0(\epsilon+1)\tau_p(\epsilon,x)$ vs x for various electron gas densities. These curves would seem to indicate that infinite τ_p values are admissible when $x=x_p$. In fact, no electron can achieve this energy loss and at the same time satisfy the energy-momentum compatibility condition. The value x_p at each value of r_s is designated by the x intercept of the vertical dashed line.

The plasmon damping effect, which takes into account the finite width of the plasma dispersion curve in the zx plane, is expected to be important primarily in the low-energy region. Although we do not expect any notable changes in the electron slowing-down spectrum, the inclusion of plasmon damping does make more efficient the numerical evaluation of Eq. (1) to obtain $\phi(E)$.

To include the plasmon damping effect in Al, we have used a simple Drude approximation to $(\epsilon^L)^{-1}$ in the neighborhood of the plasma resonance line, with coefficients taken from experiment. In this approximation, the imaginary part of the inverse dielectric function is given by

$$\mathrm{Im}\left(\frac{-1}{\epsilon_{z,x}}\right)=\frac{\gamma x x_p^2}{[x^2-x_p^2(z)]^2+\gamma^2x^2}, \tag{9}$$

where γ is a damping constant, x_p is the plasma energy in units of E_F, and $x_p(z)$ represents the plasma dispersion relation.

We have used $\hbar\gamma=1.05$ eV, $x_p=1.3558$, $E_F=11.6$ eV, and the relation

$$x_p(z)=x_p+3.54z^2+4.8z^4 \tag{10}$$

from the experiment of Swanson and Powell[16] for aluminum. Figure 5 shows results of the calculation of τ_p for several values of ϵ (dashed curves), together with the result obtained previously from the zero damping dielectric constant (the solid curve). The damping coefficient $\hbar\gamma$ is taken from the work of Swanson.[17]

The problem of obtaining numerical values for the DIMFP for the creation of secondary electrons is straightforward in principle but involves a fair amount of computation. The DIMFP $\tau_s(\epsilon,\epsilon')$ for production of a secondary electron having energy $\epsilon' E_F$ per unit energy interval about ϵ' by a primary electron of energy ϵE_F may be written[15]

$$\tau_s(\epsilon,\epsilon')=\frac{me^4k'}{\pi^3v\hbar^3}\int\frac{\delta(\epsilon-\epsilon_f-\epsilon'+\epsilon_i)}{q^4|\epsilon_{\vec{q},\omega}|^2}d\vec{k}_i d\Omega', \tag{11}$$

where $\epsilon_f E_F$ and $\epsilon_i E_F$ are the energy of the primary

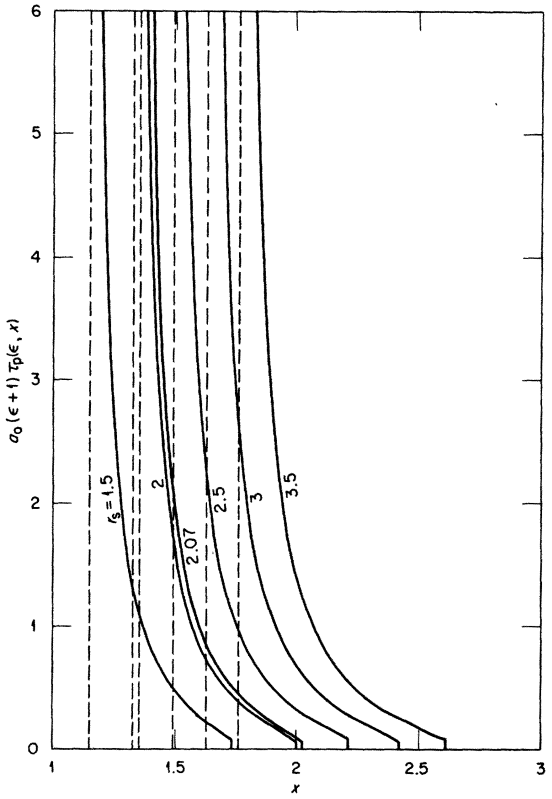

FIG. 4. Plot of $a_0(\epsilon+1)\tau_p(\epsilon,x)$ vs x in electron gases of various densities. The differential inverse mean free path $\tau_p(\epsilon,x)$ describes the probability per unit length that an electron with energy ϵE_F shall lose energy xE_F in creating a plasmon in an electron gas.

electron after the encounter and the initial energy of the struck electron, respectively. v is the velocity of the primary electron and $d\Omega'$ is the element of solid angle about the direction of the wave vector $\vec{k}'$. The integral over $\vec{k}_i$ is to be carried out over Fermi sphere of radius k_F, and $\vec{k}'$ must lie outside of this region. $\varepsilon_{\vec{q},\omega}$ is the dielectric constant of the electron gas at wave vector $\vec{q}$ and frequency ω, where one must put $\vec{q}=\vec{k}'-\vec{k}_i=\vec{k}-\vec{k}_f$ and $\omega=(\epsilon-\epsilon_f)E_F/\hbar=(\epsilon'-\epsilon_i)E_F/\hbar$. We neglect exchange scattering here.

After carrying out several integrations with changes of variable, the remaining integral for Eq. (11) may be reduced to a double integral. The sequence of operations leading to the final result is indicated in the Appendix. One finds

$$\tau_s(\epsilon,\epsilon') = \frac{\chi^2}{8a_0(\epsilon+1)}\int_{\epsilon'}^{\min(\epsilon,\epsilon'+1)} dx \int_{z_-}^{z_+} \frac{dz}{z^4|\epsilon^L_{z,x}|^2}, \quad (12)$$

where $z_\pm=\frac{1}{2}[(\epsilon'+1)^{1/2}\pm(\epsilon'+1-x)^{1/2}]$ and $\min(a,b)$ represents the smaller of the quantities a and b.

Figure 6 shows a plot of $a_0(\epsilon+1)\tau_s(\epsilon,\epsilon')$ vs ϵ' for various values of ϵ and for $r_s=2.07$. For $\epsilon \lesssim 1$ a triangular distribution in ϵ' is found.[18] As ϵ increases a strong peak develops at $\epsilon'\approx 2$. At still larger values of ϵ, the distribution in ϵ' becomes proportional to $(\epsilon')^{-2}$, again giving the expected free-electron-like distribution.

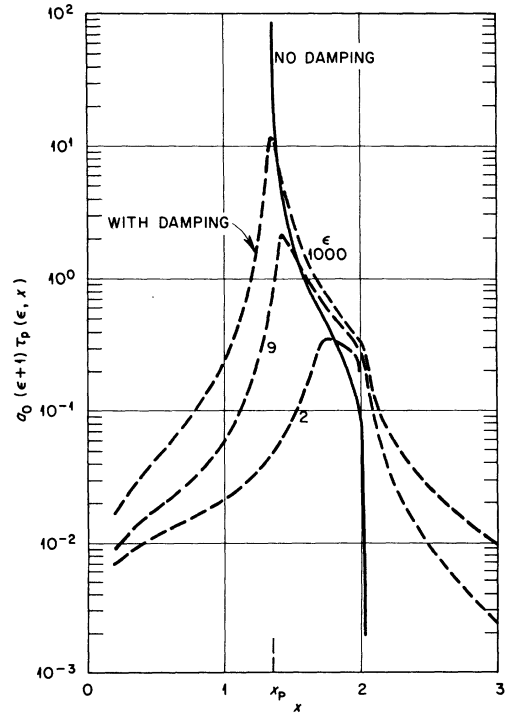

FIG. 5. Plot of $a_0(\epsilon+1)\tau_p(\epsilon,x)$ vs x in an electron gas ($r_s=2.07$). The solid curve is the result obtained from Lindhard dielectric function with no plasmon damping. Dashed curves are results obtained using the Drude dielectric function with damping coefficients taken from experiment.

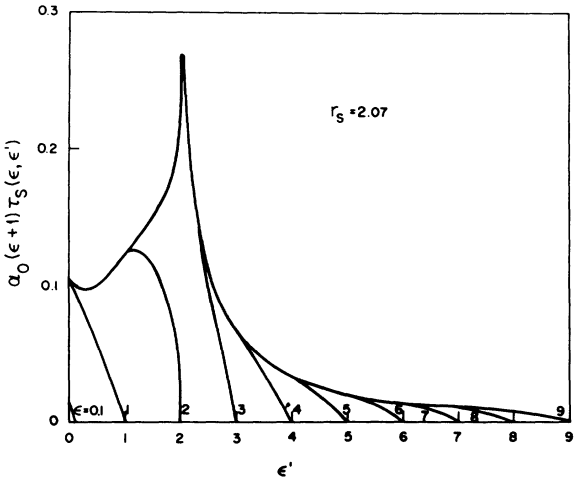

FIG. 6. Plot of $a_0(\epsilon+1)\tau_s(\epsilon,\epsilon')$ vs ϵ' in an electron gas ($r_s=2.07$). The differential inverse mean free path $\tau_s(\epsilon,\epsilon')$ describes the probability per unit length that an electron with energy ϵE_F shall create a secondary electron with energy $\epsilon' E_F$ in exciting electron-hole pairs in the electron gas.

2. *Inner shells*

We assume that excitation of all inner shells may be described in terms of atomic cross sections. Thus the DIMFP for an incident electron having energy E to lose energy $\hbar\omega$ in ionizing the ith inner shell is given in the Born approximation as

$$\tau_i(E,\omega)=n_i\left(\frac{d\sigma_i}{d\omega}\right) = \frac{2\pi n_i e^4}{E\omega}\int\frac{dk}{k}\frac{df_i}{d\omega}, \quad (13)$$

where $d\sigma_i/d\omega$ is the differential cross section per atom for the corresponding process, n_i is the number of electrons in the ith shell times the atomic density of the medium, and e is the electron charge. The generalized oscillator strength, $df_i/d\omega$, associated with the ith shell of each atom is defined by

$$\frac{df_i}{d\omega}=\frac{2m\omega}{k^2}\sum_\Omega |F_{i,\Omega}(k,\omega)|^2. \quad (14)$$

Here m is the electron mass and

$$F_{i,\Omega}=\langle\Omega,\hbar\omega-\hbar\omega_B^i|\sum_j e^{i\vec{k}\cdot\vec{r}_j}|0\rangle,$$

where $|0\rangle$ and $|\Omega,E\rangle$ are, respectively, eigenkets

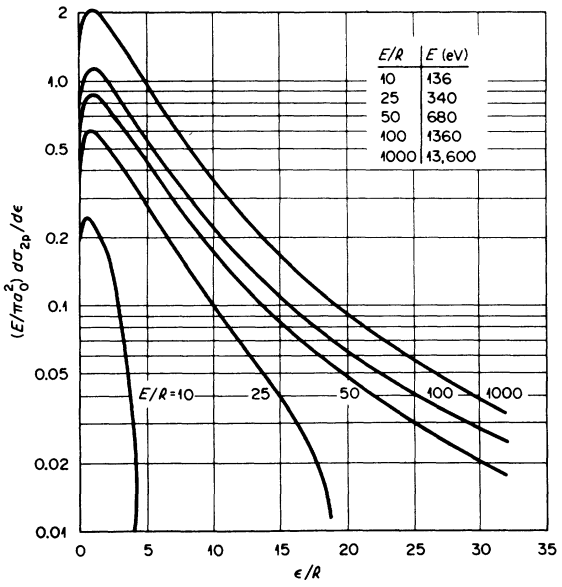

FIG. 7. Representation of $(E/\pi a_0^2)\, d\sigma_{2p}/d\epsilon$ as a function of ϵ/R for several values of electron energy E. Here $d\sigma_{2p}/d\epsilon$ is the differential cross section for ionization of the Al $2p$ shell by an electron of energy E, a_0 is the Bohr radius, and $\mathcal{R}$ is the rydberg energy ($1\mathcal{R}=13.6$ eV).

of the ground state and the ionized state which is specified by its energy E and a set Ω of all the other requisite quantum numbers. The sum over $\vec{r}_j$ runs over all coordinates of electrons in the ith shell of the atom.[19] We consider here only transitions to the continuum. Sum rule considerations given below indicate that transitions to discrete states may be neglected in this work.

Model calculations have been employed in Eq. (14) for the K and L shell of aluminum. For the K shell, we have used the hydrogenic model.[20] For aluminum $L_{\rm I}$ and $L_{\rm II,III}$ subshells, we have employed the numerical results of Manson,[21] which were based on a Hartree-Slater central field potential model. Figure 7 shows some representative results of the model calculation for differential cross sections for the ionization of aluminum $L_{\rm II,III}$ subshell. Note that the energy loss by the incident electron in exciting this shell is given by $\hbar\omega=\epsilon+5.95\mathcal{R}$, where $5.95\mathcal{R}$ is the binding energy of the $L_{\rm II,III}$ subshell of aluminum and $\mathcal{R}=13.6$ eV is the rydberg energy.

3. *Auger electrons*

When an inner-shell electron is removed from an ion core, the vacancy it leaves is filled within 10^{-17} to 10^{-12} sec by an electron from an outer shell.[22] The energy liberated in this transition may be taken up by the radiation field or it may be absorbed in the creation of an Auger electron, or in the generation of intershell Auger cascades.[23] For low-Z materials, the emission of Auger electrons is more likely than photon emission.[23] For present purposes, we neglect details of the Auger processes and assume that Auger electrons are produced by filling of a hole in a given shell by an electron from the adjacent shell with smaller binding energy. The contribution to the electron slowing-down spectrum from Auger electrons is thus obtained by adding monoenergetic electron sources, $\mathfrak{N}(E_i)\,\delta(E-E_i)$, at various characteristic Auger energies, E_i, to Eq. (1). Here the Auger source density at energy E_i is given by

$$\mathfrak{N}(E_i)=\sum_j M_{ij}\int_0^\infty \mu_j(E)\phi(E)\,dE\,, \tag{15}$$

where M_{ij} is the number of Auger electrons produced with energy E_i following the creation of a vacancy in the jth shell, and $\mu_j(E)$ is the electron inverse mean free path at energy E for the ionization of electrons from the jth shell. The matrix M_{ij} is determined as follows. In this work, for example, we have considered the filling of a vacancy in the Al K shell by an electron from the Al $L_{\rm II,III}$ subshell. The filling will create an Auger electron having energy $E_K\simeq\hbar\omega_B^K-2\hbar\omega_B^{L_{\rm II,III}}$ and will give rise to two holes in the Al $L_{\rm II,III}$ subshell. Then each of the Al $L_{\rm II,III}$ subshell vacancies will give rise to two holes in the conduction band and an Auger electron with energy $E_{L_{\rm II,III}}\cong\hbar\omega_B^{L_{\rm II,III}}-E_F$. Therefore, $M_{K,K}=M_{L_{\rm II,III},L_{\rm II,III}}=1$ and $M_{L_{\rm II,III},K}=2$. We thus account for intershell Auger cascades in a schematic way which should be accurate enough for our purposes.

We neglect Auger electrons from the filling of holes in the conduction band since these will become important primarily for energies very close to the Fermi energy. Ritchie[24] has studied the characteristics of electron-hole cascades in this region. Gadzuk and Plummer[25] have found experimental evidence for such cascades in field-emission work.

B. Inverse mean free paths

Individual contributions to the electron inverse mean free path (IMFP) from each inelastic collision process are obtained by integration of the corresponding DIMFP over the energy transfer. Inelastic collisions resulting in excitation of inner-shell electrons to discrete energy levels have not been considered. These collisions contribute negligibly to the total oscillator strength as may be demonstrated using the sum rule[19] $Z_i=\int_0^\infty df_i/d\omega\,d\omega$, where Z_i is the number of electrons per atom in the ith inner shell. If one integrates the GOS function for a given shell at a given momentum transfer over a sufficiently wide energy transfer region, one finds that the theoretically expected total oscil-

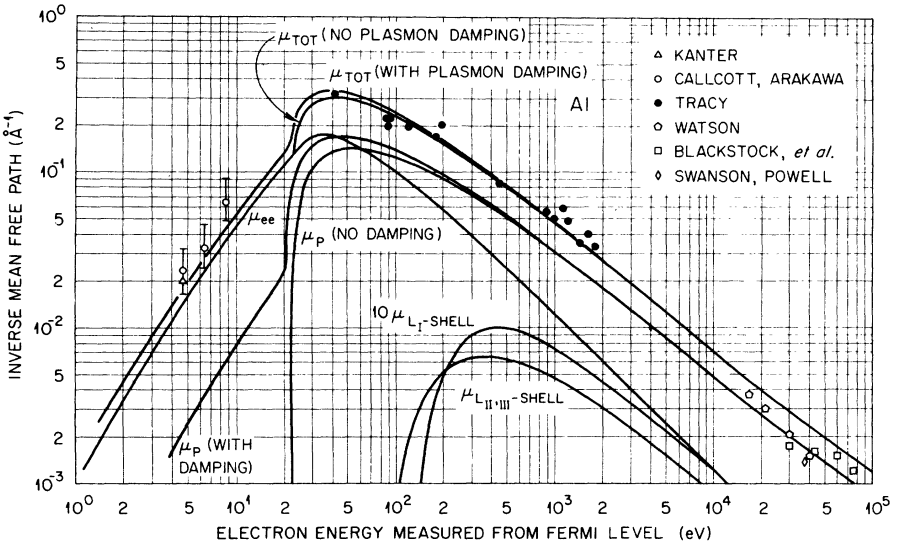

FIG. 8. Inverse mean free path (IMFP) of electrons vs electron energy in Al metal. The electron gas model is used to compute μ_{ee}, the IMFP for electron-hole pair creation, and μ_p, the IMFP for plasmon creation, for conduction band electrons taking $r_s = 2.07$. As described in the text, μ_p is computed both including damping and neglecting it. The IMFP for generation of a vacancy in the L_I shell, μ_{L_I}, and that for the $L_{II,III}$ shell, $\mu_{L_{II,III}}$, are computed from atomic models. μ_{TOT} is the total IMFP. Data from experimental measurements of the attenuation length of electrons in Al, from various sources (see text), are included. μ_K is so small that it does not show on this plot.

lator strength has already been used up by the ionization process which leaves very little oscillator strength for discrete excitations. In our model calculations, we found that $f_K = 2.0$ for the aluminum K shell and $f_{L_I} + f_{L_{II,III}} = 8.0$, where $f_i = \int_0^\infty d\omega (df_i/d\omega)$, essentially independent of momentum transfer. Figure 8 shows the results of our calculations of the IMFP versus electron energy using the models described above for the inelastic collision processes in aluminum. Results for energies above 10 keV have been corrected for relativistic effects in an approximate way by replacing the kinetic energy E in the denominator of Eqs. (13) and (3) by $(\frac{1}{2}mv^2)$, which relates to E by $\frac{1}{2}mv^2 = \frac{1}{2}mc^2[1-(1+E/mc^2)^{-2}]$, where c is the speed of light.

Some experimental values from a number of different experiments are also plotted in Fig. 8. The points at large incident energy ($\gtrsim 10^4$ eV) are taken from measurements of the mean free path for plasmon emission.[16,26,27] Those at intermediate energy (50–1500 eV) were inferred from measured escape depths for Auger electrons,[28] while the points at energies less than ~10 eV relative to the Fermi level were inferred from transmission and photoemission measurements.[29,30]

IV. NUMERICAL METHODS AND RESULTS

Although Eq. (1) appears simple, the task of obtaining solutions from it is by no means straightforward because numerous inelastic DIMFP functions over a wide energy region are employed and their cumulative contributions to the slowing-down fluxes require careful consideration. The standard numerical method for solving the equation involves approximating the integrals as sums and using a suitable integration formula, e.g., the Simpson's rule, for the integrals. However, it is impractical to use this direct method for the computation of electron slowing-down spectra over the wide range of energies which the Keplertron data covers. The work would require very large computing times due to the small energy mesh size needed for accurate evaluations.

Before describing solutions corresponding to large source energies, it is interesting to discuss electron slowing-down spectra for low-energy monoenergetic sources in which inner-shell ionizations are not important. In this case, $N(E)$ is replaced by $\delta(E-E_0)$ in Eq. (1) and the direct numerical method may be employed. We have used Simpson's rule to convert the integrals of Eq. (1) to sums at energies when the summation runs over odd energy points, and trapezoidal rule over the first interval and Simpson's rule over the remaining intervals at energies when even points are summed.[1,2]

The solid curves of Fig. 9 show plots of the slowing-down flux $\phi(\epsilon)$ against ϵ for an electron gas with $r_s = 2.07$ due to sources of monoenergetic electrons with energies $\epsilon_0 = 5$, 10, 15, 20. The flux is normalized to a source density of one electron per Å^3 emitted per unit time. The peaks just below the source energy correspond to electrons that have

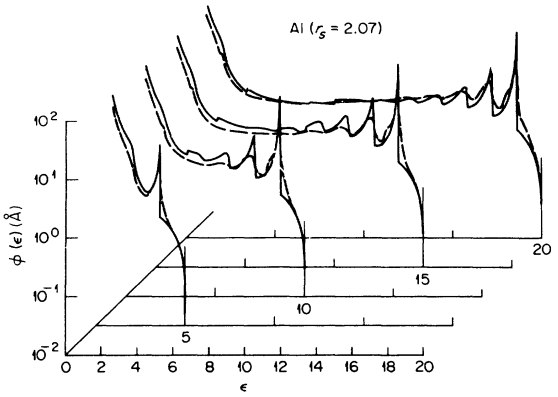

FIG. 9. Electron slowing-down flux, $\phi(\epsilon)$ in an electron gas of $r_s = 2.07$ due to sources of monoenergetic electrons with energies $\epsilon_0 = 5$, 10, 15, 20. Solid curves are results without plasmon damping included.

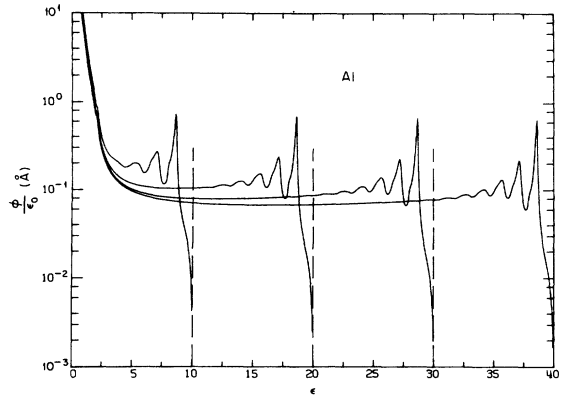

FIG. 11. Computed electron flux spectrum $\phi(\epsilon)$ divided by ϵ_0 for monoenergetic sources with energies $\epsilon_0 = 10$, 20, 30, and 40 in Al metal. The contribution from inner shells is included. Plasmon damping is taken into consideration.

generated one, two, three, etc., plasmons in succession. After several fluctuations as ϵ decreases, the flux becomes fairly smooth. In the region of energy close to the Fermi level, the flux shows a strong divergence, due to the fact that secondary electrons are generated copiously in this region. In the same figure, the results of calculations of $\phi(\epsilon)$ with the inclusion of plasmon damping are shown as dashed curves corresponding to the same source energies. The damping effect smooths the plasmon loss peaks to some extent and, in addition, shows somewhat smaller fluxes at the lower-energy region, compared to the undamped results. The latter effect may be attributed to the larger stopping power obtained in that energy region for the damped case.[1,2]

Figure 10 is a plot of the slowing-down flux $\phi(\epsilon)$ against ϵ for a monoenergetic electron source with energy $\epsilon_0 = 40$ in Al metal, where curves B and A represent, respectively, results calculated with and without the contribution from excitation of inner shells. In both cases, we have employed the DIMFP for plasmon generation with plasmon damping considered. For high energies, the slowing-down flux $\phi(\epsilon)$ is actually smaller when the contribution from inner shells is included than when it is neglected. As energy decreases, inner shells begin to make positive contribution.

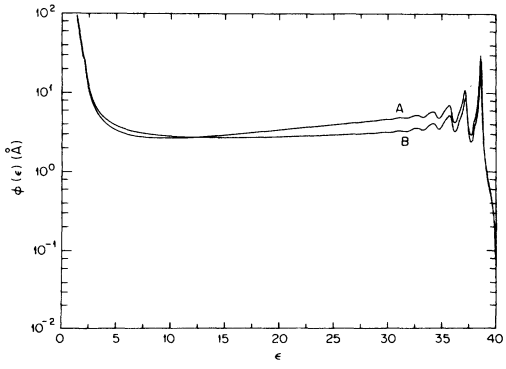

FIG. 10. Electron slowing-down flux in Al metal due to a monoenergetic electron source with energy $\epsilon_0 = 40$. Curves B and A represent, respectively, results calculated with and without the contribution from inner shells.

Figure 11 shows the result of computed electron flux spectrum $\phi(\epsilon)$ divided by ϵ_0 for monoenergetic sources with energies $\epsilon_0 = 10$, 20, 30, and 40 in Al metal. Here again we have used the DIMFP for plasmon generation for the damped case, and the contribution from excitation of inner shells is also included.

To find electron slowing-down spectra accurately and efficiently over the wide energy range covered by the Keplertron measurement, modifications of Eq. (1) and the numerical procedure are both necessary. First, electron slowing-down spectra obtained by Spencer and Fano,[1,2] who used the continuous slowing-down approximation and the Møller scattering cross section, are valid for energies greater than several times the binding energy of the most tightly bound inner shell. For aluminum, the binding energy of the K shell is ~114 Ry. Thus, we have assumed that electron slowing-down spectra obtained by the Spencer-Fano method were correct for energies above $E_0 = 10$ keV. To solve for the electron flux at energies below 10 keV, one adds to the source flux $N(E)$ in Eq. (1) an equivalent source flux $S_{SF}(E)$ obtained from the calculation of the integral on the right-hand side of this equation integrated between E_0 and infinity. Electron flux

at energies below E_0 may then be calculated from solving Eq. (1), starting with a solution at E_0, according to the distribution of the new source flux, $S(E) = N(E) + S_{SF}(E)$. Figure 12 shows a plot of the function $S_{SF}(E)$ vs E computed from a Spencer-Fano flux appropriate to electrons from ^{198}Au β particles liberated in aluminum metal. This flux distribution was computed from the Spencer-Attix equation,[2] assuming an allowed β spectrum. Here we have normalized the flux to one electron born per unit volume. At high energies, most of the contribution to the flux is from degraded "Spencer-Fano" flux electrons above E_0. As the electron

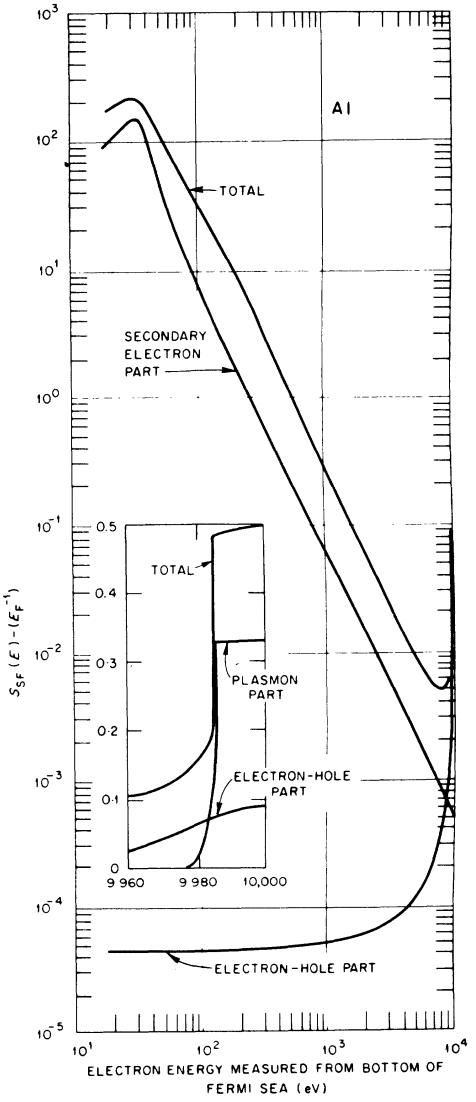

FIG. 12. First collision electron source density $S_{SF}(E)$ in Al, calculated from differential inverse mean-free-path functions derived in this work, and from Spencer-Fano flux for electron energy above 10 keV.

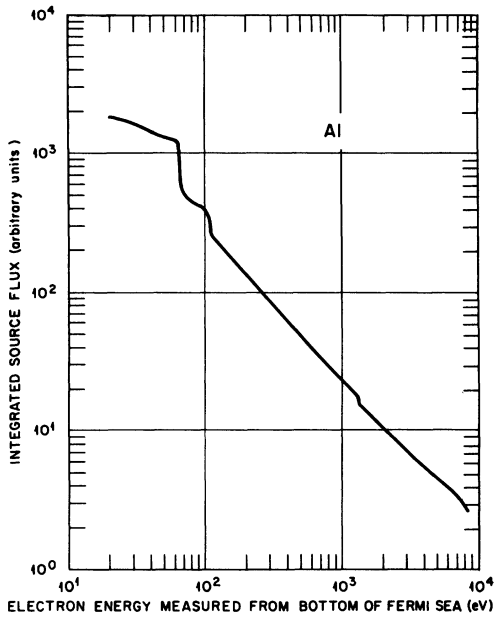

FIG. 13. Plot of the integrated source flux [described in Eq. (16)] as a function of electron energy. Auger electron contributions are included.

energy decreases immediately below E_0, the flux also decreases and reaches a minimum value. It then rises steeply as energy further decreases. A detailed plot of the source flux for energies close to E_0, shown on the bottom left corner of the figure, is needed for close examination because the plasmon contribution only extends over a limited energy region below E_0. The curve drops sharply for energies below $E_0 - E_p$ and contains no plasmon contribution when E is less than $E_0 - 2.02\,E_F$, where 2.02 is the cutoff value shown in Fig. 4 for $r_s = 2.07$.

As mentioned at the beginning of this chapter, the direct numerical solution of Eq. (1) is impractical for the present calculation because of the discontinuity of the plasmon contribution to the new source flux. These difficulties may be resolved by transforming both sides of Eq. (1) into integrated forms.[1] Integrating Eq. (1) over the energy between E and E_0, one gets

$$\int_E^{E_0} \phi(E')\left(\int_{E'-E}^{E'} \tau(E', E_1)\,dE_1 - \int_E^{E'} \tau_s(E', E_1)\,dE_1\right)dE' = \int_E^{E_0} S(E')\,dE' + \sum_i \int_E^{E_0} \mathfrak{N}(E_i)\,\delta(E' - E_i)\,dE', \tag{16}$$

where the second term on the right-hand side is due to Auger electron contributions.

Figure 13 shows a plot of the integrated source flux, i.e., the right-hand side Eq. (16), as a func-

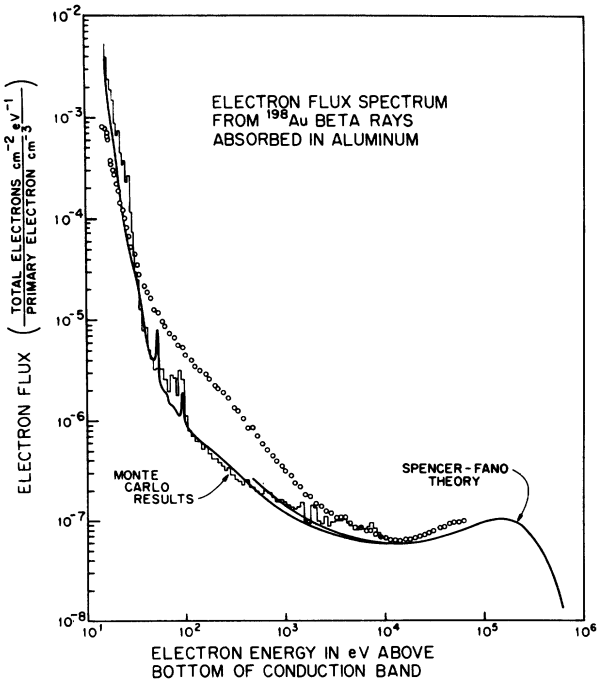

FIG. 14. Electron slowing-down spectrum in Al metal due to ^{198}Au β rays. Solid curve is the result of present calculations. Histogram is the spectrum calculated from a Monte-Carlo code. Experimental values are shown as open circles. The Spencer-Fano flux at higher energies is shown as a solid line.

tion of E. The curve increases almost linearly on a logarithmic plot as the energy decreases. Auger electron contributions occur at ~1380 eV for the transition from the $L_{\text{II,III}}$ subshell to the K shell, ~100 eV from the conduction band to the L_{I} subshell, and ~65 eV from the conduction band to the $L_{\text{II,III}}$ subshell.

We have employed Eq. (16) using a modified numerical method, i.e., applied Simpson's and trapezoidal rules to the function $\phi(E')$ rather than to the integrand itself. The procedure is as follows. After converting the integrals over E' in Eq. (16) into sums, we let $E = E_j = E_0 - j\Delta$, where Δ is an energy mesh size. To calculate the flux $\phi(E)$ at energy E, we have assumed a parabolic expression $\phi(E') = aE'^2 + bE' + c$ for the fitting of the function ϕ over the region between $E' = E_j$ and E_{j-2}, where a, b, and c are determined by applying Simpson's rule to ϕ over energies $E' = E_j$, E_{j-1}, and E_{j-2}. If the mesh size is greater than the cutoff plasmon energy, the rest of the sum over E' between E_{j-3} and E_0 may be evaluated using conventional Simpson's and trapezoidal rules for the integral. The modification is necessary if one uses a bigger mesh size for energies because again the plasmon contribution to the integrand extends only over a limited energy range. The modified technique has been applied to compute electron slowing-down spectra in aluminum down to energies of several hundred eV. At still lower energies, slowing-down spectrum is shown in Fig. 14 together with the theoretical result from a Monte-Carlo calculation[14] and experimental data on the slowing-down flux of electrons from ^{198}Au β rays in aluminum metal. The first Auger electron contribution to the theoretical curve at ~1380 eV can be seen just barely from the figure. Other Auger electrons contribute to the flux at ~100 eV and ~65 eV. The vertical ticks at 110 eV and at 75 eV represent uncollided Auger electrons and correspond to 1.24×10^2 and 3.0×10^2 electrons emitted per cm^3, respectively. The first and second plasmon satellites of these electrons are plainly seen. The two theoretical curves agree better with each other than with the experiment. The small differences between the theoretical results for energies between 10^3 and 10^4 eV are due to the different models and methods of solution employed. The fairly good agreement between theories over the wide energy range suggests that a re examination of the experimental data is necessary.

V. DISCUSSION

We have determined distributions in energy of electrons slowing down in Al metal by employing the Boltzmann transport equation. Various models for different shells of electrons were used to obtain theoretical inelastic differential inverse mean free paths for this work. Energy flux spectra were computed for both monoenergetic electron sources and for β particles from the decay of radioactive ^{198}Au in Al metal. The agreement between our model calculations and experimental measurements using the Keplertron is fairly good, especially with respect to the magnitudes of these two in the high-energy region. The consistent discrepancies between theory and experiment in the low- and intermediate-energy regions[32] require further study.

In this work, we have neglected the quasicontinuous energy loss by electrons due to phonon generation in the metal. We expect these processes to be quite unimportant compared with electronic excitations until electrons have slowed to energies close to the Fermi level. Similarly, contributions from Auger electron-hole cascade processes in the valence band should be negligible[32] until energies are quite small. We have neglected the generation of surface plasmons and nonlinear effects due to interaction among excited electrons and holes.

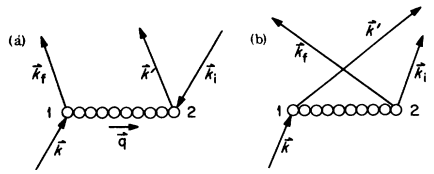

FIG. 15. Feynman diagrams representing processes by which a hot electron may lose energy to a free electron gas. (a) shows a direct process and (b) shows an exchange scattering.

These omissions should have little effect upon the computed slowing-down fluxes under conditions existing in the experiments with which we compare.

ACKNOWLEDGMENTS

We are indebted to Dr. S. T. Manson for his generosity in supplying us with the numerical values of generalized oscillator strengths for transitions from the inner shells of the Al atom. The support and encouragement of our colleagues, J. C. Ashley, R. D. Birkhoff, J. A. Bradford, and E. A. Burke are gratefully acknowledged. In addition, V. E. Anderson was of great assistance in some of the numerical work done in this project.

APPENDIX: DERIVATION OF DIMFP FOR THE GENERATION OF SECONDARY ELECTRONS FROM AN ELECTRON GAS

The process which will be considered is shown in the Feynman diagram of Fig. 15(a). An incident electron with momentum $\hbar\vec{k}$ interacts with electrons in the Fermi sea. The polarization propagator which describes the process is given by

$$G(2,1)=\frac{1}{2\pi L^3}\sum_{\vec{q}}\int d\omega\,\frac{4\pi}{q^2\epsilon_{\vec{q},\omega}}\times\exp[i(\vec{q}\cdot\vec{r}_{21}-\omega t_{21})],\quad(17)$$

where $\vec{r}_{21}=\vec{r}_2-\vec{r}_1$, $t_{21}=t_2-t_1$, and L^3 is the volume used for normalizations.

We will neglect the exchange process shown in Fig. 15(b). Kleinman[11] concludes that contributions from this process are canceled by higher-order corrections to the IMFP.

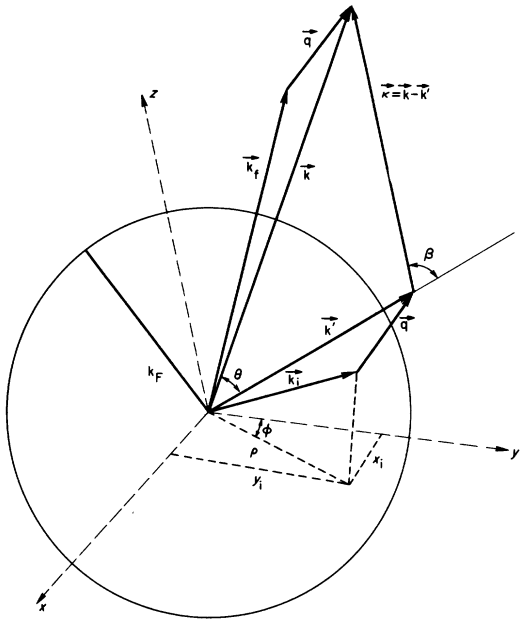

FIG. 16. Momentum diagram for the scattering process shown in Fig. 15 (a).

The DIMFP $\tau_s(\epsilon,\epsilon')$ for production of a secondary electron having energy $\epsilon' E_F$ by a primary electron of energy ϵE_F is given by Eq. (11). The integration region over $\vec{k}_i$ and Ω' may be represented by the momentum diagram for the scattering process as shown in Fig. 16. One may carry out one of the k_i integrals immediately by utilizing the δ function

$$\delta(\epsilon-\epsilon_f-\epsilon'+\epsilon_i)=\delta\left[\frac{\hbar^2}{mE_F}\vec{\kappa}\cdot(\vec{k}'-\vec{k}_i)\right],\quad(18)$$

where $\vec{\kappa}=\vec{k}-\vec{k}'$, the expression $\vec{k}_f=\vec{k}-\vec{k}'+\vec{k}_i$ and the relations between energy and wave vector for a free electron have been used. If one erects a system of Cartesian coordinates with origin 0 at the center of the Fermi sphere, the z axis parallel to the vector $\vec{\kappa}$, and $\vec{k}'$ and $\vec{k}$ lying in the yz plane, Eq. (11) then becomes

$$\tau_s(\epsilon,\epsilon')=\frac{2me^4}{\pi^2 v\hbar^3}\int dx_i\int dy_i\int\sin\theta'\,d\theta'\left(\frac{mE_F k'}{\hbar^2\kappa q^4|\epsilon_{q,\omega}|^2}\right)_{z_i=k'\cos\beta},\quad(19)$$

where (x_i, y_i, z_i) are the components of the vector $\vec{k}_i$ in this system.

The integrals over x_i and y_i are to be carried out over the circular area enclosed on a plane parallel with the xy plane and at a distance $k'\cos\beta$ from the origin formed by the intersection of the Fermi sphere with that plane. One may convert from the variables (x_i, y_i) to polar variables (ρ,ϕ) and utilize the relation $\sin\theta'\,d\theta'=(\kappa/k)\sin\beta\,d\beta$. Equation (19) then becomes

$$\tau_s(\epsilon,\epsilon')=\frac{2m^2e^4E_F}{\pi^2 v\hbar^5}\int_{\cos^{-1}(k_F/k')}^{\pi-\cos^{-1}(k_F/k')}\sin\beta\,d\beta\int_0^{(k_F^2-k'^2\cos^2\beta)^{1/2}}\rho\,d\rho\int_0^{2\pi}d\phi\left(\frac{k'}{kq^4|\epsilon_{q,\omega}|^2}\right).\quad(20)$$

Here q^2 and ω may be explicitly expressed in terms of ρ, ϕ, and β due to the relations $\vec{q}=\vec{k}-\vec{k}_i$ and $\omega=\hbar/2m(k'^2-k_i^2)$ as

$$q^2=k'^2\sin^2\beta+\rho^2-2\rho k'\sin\beta\cos\phi\,, \tag{21}$$

and

$$\omega=(\hbar/2m)(k'^2\sin^2\beta-\rho^2)\,. \tag{22}$$

Changing variables to $z=q/2k_F$, $x=\hbar\omega/E_F$, ϵ, ϵ', $r=\rho/k_F$, and $\nu=(k'/k_F)\cos\beta$, Eqs. (20)–(22) become

$$\tau_s(\epsilon,\epsilon')=\frac{1}{8a_0(\epsilon+1)}\frac{k_Fe^2}{\pi^2\hbar}\times\int_0^1 d\nu\int_0^{(1-\nu^2)^{1/2}} r\,dr\int_0^{2\pi}\frac{d\phi}{z^4|\varepsilon_{z,x}|^2}\,, \tag{23}$$

$$z^2=\tfrac{1}{4}[x'-\nu^2+r^2-2r(x'^2-\nu^2)^{1/2}\cos\phi]\,, \tag{24}$$

and

$$x=x'-\nu^2-r^2\,. \tag{25}$$

Equation (23) may be simplified by changing variables from (r,ν) to $[\zeta=(r^2+\nu^2)^{1/2},\ \lambda=r/\zeta]$ and then from (ζ,ϕ) to (x,z). After interchanging the order of the λ and z integrals, one finds

$$\tau_s(\epsilon,\epsilon')=\frac{\chi^2}{8a_0(\epsilon+1)}\int_{\epsilon'}^{\min(\epsilon,\epsilon'+1)}dx\times\int_{[(\epsilon'+1)^{1/2}-(\epsilon'+1-x)^{1/2}]/2}^{[(\epsilon'+1)^{1/2}+(\epsilon'+1-x)^{1/2}]/2}\frac{dz}{z^4|\varepsilon_{z,x}|^2}\,. \tag{26}$$

Equation (26) has been used for numerical evaluation of the DIMFP for the creation of secondary electrons in the electron gas.

It may be verified from Eqs. (3) and (26) that the IMFP for scattering of a primary electron to all allowed lower energies by electron-hole pair creation is identically equal to the IMFP for the production of secondary electrons of all possible energies. That is

$$\int_0^{\epsilon}\tau_s(\epsilon,\epsilon')\,d\epsilon'=\int_0^{\epsilon}\tau_{ee}(\epsilon,\epsilon')\,d\epsilon'\,. \tag{27}$$

---

†Present address: Health Physics Section, National Tsing Hua University, Hsinchu, Taiwan 300, Republic of China.

*Research sponsored in part by the Energy Research and Development Administration under contract with Union Carbide Corporation and in part by the Deputy for Electronics Technology, Air Force Systems Command under Contract No. Y77-6.

[1]L. V. Spencer and U. Fano, Phys. Rev. 93, 1172 (1954).
[2]L. V. Spencer and F. H. Attix, Radiat. Res. 3, 239 (1955); see also R. T. McGinnies, U.S. Natl. Bur. Stand. Circular No. 597, 1959 (unpublished).
[3]U. Fano and L. V. Spencer, Int. J. Rad. Phys. Chem. 7, 63 (1975).
[4]R. L. Platzman, *Radiation Research*, edited by G. Silini (North-Holland, Amsterdam, 1967), p. 20.
[5]D. A. Douthat, Radiat. Res. 65, 1 (1975).
[6]S. C. Soong, Radiat. Res. 67, 187 (1976).
[7]W. J. McConnell, H. H. Hubbell, Jr., R. N. Hamm, R. H. Ritchie, and R. D. Birkhoff, Phys. Rev. 138, A1377 (1965).
[8]L. C. Emerson, R. D. Birkhoff, V. E. Anderson, and R. H. Ritchie, Phys. Rev. B 7, 1798 (1973).
[9]L. Pages, E. Bertel, H. Joffre, and L. Sklavenitis, At. Data 4, 1 (1972).
[10]J. Lindhard, K. Dan. Vidensk. Selsk. Mat.-Fys. Medd. 28, 1 (1954).
[11]L. Kleinman, Phys. Rev. B 2, 2982 (1971).
[12]A. P. Pathak and M. Yussouff, Phys. Status Solidi B 49, 431 (1972).
[13]D. Penn, Phys. Rev. B 13, 5248 (1976).
[14]A. W. Overhauser, Phys. Rev. B 3, 1888 (1971).
[15]R. H. Ritchie, Phys. Rev. 114, 644 (1959).
[16]N. Swanson and C. J. Powell, Phys. Rev. 145, 197 (1966).
[17]N. Swanson, J. Opt. Soc. Am. 54, 1130 (1964).
[18]R. H. Ritchie and J. C. Ashley, J. Phys. Chem. Solids 26, 1689 (1965).
[19]M. Inokuti, Rev. Mod. Phys. 43, 297 (1972).
[20]E. Merzbacher and H. W. Lewis, *Handbuch der Physik XXXIV* (Springer-Verlag, Berlin, 1958).
[21]S. T. Manson, Phys. Rev. A 6, 1013 (1972).
[22]E. Bauer, Vacuum 22, 539 (1972).
[23]T. A. Carlson, Phys. Today 25, 30 (1972).
[24]R. H. Ritchie, J. Appl. Phys. 37, 2276 (1966).
[25]J. W. Gadzuk and E. W. Plummer, Phys. Rev. Lett. 26, 92 (1971).
[26]A. W. Blackstock, R. H. Ritchie, and R. D. Birkhoff, Phys. Rev. 100, 1078 (1955).
[27]H. J. Watson, Ph.D. thesis (University of Florida, Gainsville, 1962) (unpublished).
[28]J. C. Tracy, J. Vac. Sci. Technol. 11, 280 (1974).
[29]H. Kanter, Phys. Rev. B 1, 522 (1970).
[30]T. A. Callcott and E. T. Arakawa, Phys. Rev. B 11, 2750 (1975).
[31]For a Monte-Carlo calculation, see e.g., M. J. Berger, *Methods in Computational Physics* (Academic, New York, 1963), Vol. 1, p. 135.
[32]R. H. Ritchie, C. J. Tung, V. E. Anderson, and J.C. Ashley, Radiat. Res. 64, 181 (1975).